Journal of Hazardous Materials 418 (2021) 126294

Contents lists available at ScienceDirect

Journal of Hazardous Materials

journal homepage: www.elsevier.com/locate/jhazmat

Research Paper

Fe-based single-atom catalysis for oxidizing contaminants of emerging concern by activating peroxides

Zhe Zhou [a], Mengqiao Li [a], Chunguang Kuai [b], Yuxin Zhang [b], Virginia F. Smith [c], Feng Lin [b], Ashlee Aiello [c], David P. Durkin [c,*], Hanning Chen [d,*], Danmeng Shuai [a,*,1]

[a] Department of Civil and Environmental Engineering, The George Washington University, Washington, DC 20052, USA
[b] Department of Chemistry, Virginia Tech, Blacksburg, VA 24061, USA
[c] Department of Chemistry, United States Naval Academy, Annapolis, MD 21402, USA
[d] Department of Chemistry, American University, Washington, DC 20016, USA

ARTICLE INFO

Editor: Dr. B. Lee

Keywords:
Single-atom catalysis
Electronic structure
High-valent Fe species
Contaminants of emerging concern
Peroxymonosulfate

ABSTRACT

We prepared a single-atom Fe catalyst supported on an oxygen-doped, nitrogen-rich carbon support (SAFe-OCN) for degrading a broad spectrum of contaminants of emerging concern (CECs) by activating peroxides such as peroxymonosulfate (PMS). In the SAFe-OCN/PMS system, most selected CECs were amenable to degradation and high-valent Fe species were present for oxidation. Moreover, SAFe-OCN showed excellent performance for contaminant degradation in complex water matrices and high stability in oxidation. Specifically, SAFe-OCN, with a catalytic center of Fe coordinated with both nitrogen and oxygen (FeN_xO_{4-x}), showed 5.13-times increased phenol degradation kinetics upon activating PMS compared to the catalyst where Fe was only coordinated with nitrogen (FeN_4). Molecular simulations suggested that FeN_xO_{4-x}, compared to FeN_4, was an excellent multiple-electron donor and it could potential-readily form high-valent Fe species upon oxidation. In summary, the single-atom Fe catalyst enables efficient, robust, and sustainable water and wastewater treatment, and molecular simulations highlight that the electronic nature of Fe could play a key role in determining the activity of the single-atom catalyst.

1. Introduction

Contaminants of emerging concern (CECs) found in an aquatic environment can potentially pose risks to humans and ecological systems (Mawhinney et al., 2011; Fu et al., 2019; Patel et al., 2019). Due to their environmental persistence and trace level concentrations, conventional water and wastewater treatment cannot remove CECs efficiently (Wang and Wang, 2016; Patel et al., 2019). Activated carbon adsorption and nanofiltration/reverse osmosis are employed to retain CECs (Ternes et al., 2002; Shannon et al., 2008; Patel et al., 2019); but further treatment or disposal of exhausted adsorbents or concentrated brine is needed (Bartolomeu et al., 2018). Advanced oxidation processes (AOPs) have emerged as a promising technology for degrading CECs by taking advantage of reactive oxygen species (ROS), such as hydroxyl radical ($^{\bullet}OH$), sulfate radical ($SO_4^{\bullet-}$), and singlet oxygen ($^1O_2$) (O'Shea and Dionysiou, 2012; Lee et al., 2020).

$^{\bullet}OH$ is the most powerful oxidant for water treatment ($E = 1.9–2.7$ V) and it non-selectively attacks most organics at a near diffusion-controlled rate (10^{10} M^{-1} s^{-1}) (Buxton et al., 1988; Lee and von Gunten, 2010; Lian et al., 2017; Nosaka and Nosaka, 2017; Lee et al., 2020). $SO_4^{\bullet-}$ ($E = 2.5 – 3.1$ V) is also capable of decomposing many CECs (Lian et al., 2017; Lee et al., 2020; Wang et al., 2019). Unfortunately, the presence of natural organic matter (NOM) and inorganic anions (e.g., CO_3^{2-}, HCO_3^-, and Cl^-) in water can significantly lower the reactivity of $^{\bullet}OH/SO_4^{\bullet-}$ towards CECs (Oh et al., 2016; Lee et al., 2020; Wojnarovits et al., 2020). Moreover, these radicals can form toxic byproducts, such as trihalomethanes, bromate, and chlorate, which compromise the safety of treated water (Oh et al., 2016; Lee et al., 2020). In addition, due to the poor radical production efficiency and low selectivity of the radicals, a large amount of oxidants (e.g., hydrogen peroxide (H_2O_2) and peroxydisulfate (PDS)) is needed to maintain a reasonable steady-state concentration of the radicals for water purification, which is costly and not sustainable (Brame et al., 2015). Last but not least, catalytic materials used in radical-based AOPs could be sacrificed by radical attack,

* Corresponding authors.
E-mail addresses: durkin@usna.edu (D.P. Durkin), hchen@american.edu (H. Chen), danmengshuai@gwu.edu (D. Shuai).
[1] Website: http://materwatersus.weebly.com/

https://doi.org/10.1016/j.jhazmat.2021.126294
Received 31 March 2021; Received in revised form 21 May 2021; Accepted 31 May 2021
Available online 2 June 2021

resulting in decreased long-term reactivity (Marin et al., 2012). Because of the limitations of radical-based AOPs, the use of nonradical-driven reactions for CEC degradation are attracting attention.

Nonradical-based oxidation processes have been developed for decomposing CECs in photocatalysis, electrocatalysis, and peroxide-driven reactions, but a low reduction potential of $^1O_2$ (E^0 = 0.65 V) limits its application (Nosaka and Nosaka, 2017; Lee et al., 2020). Electron transfer from organic contaminants to peroxides mediated by conductive catalysts is another possible mechanism for nonradical-driven reactions (Yun et al., 2018; Lee et al., 2020). However, $^1O_2$-based oxidation processes and catalyst-mediated electron-transfer are at their nascent stage and thus have not been used for large-scale water purification. High-valent metal species including ferrate (Fe^{VI}) and permanganate (Mn^{VII}) are long-established oxidants for water and wastewater treatment, although they produce metal-containing sludges that require further disposal (Hu et al., 2010; Sharma et al., 2015; Li et al., 2018b; Chen et al., 2019).

Bioinspired catalysts leveraging high-valent transition metals for nonradical-driven oxidation of contaminants have been proposed, developed, and implemented (Collins and Ryabov, 2017; Lee et al., 2020). In nature, during the catalytic cycle of peroxidases and cytochrome P450 enzymes, high-valent Fe species ($Fe^{IV/V}$=O) are produced at the active site of FeN_x via the heterolytic cleavage of the O-O bond in $Fe^{II/III}$-O-O-R intermediates (Chen et al., 2018; Fasan, 2012; Rana et al., 2015). Fe-tetraamidomacrocyclic-ligand activators (Fe-TAMLs) were one of the first bioinspired catalysts that have been used for CECs removal by activating peroxides (e.g., H_2O_2 and PMS) and forming $Fe^{IV/V}$=O (Collins and Ryabov, 2017; Gupta et al., 2002; Kundu et al., 2013; Li et al., 2018a). However, Fe-TAMLs are water soluble, and immobilization or separation of the catalyst is essential for practical water applications, highlighting the need for heterogenous bioinspired catalysts. Currently, single-atom catalysts (SACs) are emerging as excellent candidates for mimicking peroxidases and cytochrome P450 enzymes (Jiao et al., 2020; Kaiser et al., 2020). As the new frontier in heterogenous catalysis, SACs show promise for use in organic synthesis, renewable energy production, and environmental remediation. The favorable properties of SACs include 100% of metal dispersion, well-engineered coordination environment of the catalytic center, specific interactions between reactants and the catalysts, and high stability and reusability of the catalysts (Cui et al., 2018; Liu, 2017; Yan et al., 2018). Nitrogen-rich materials that can provide abundant nitrogen-coordination sites for maximum deposition of single metal atoms have been selected for preparing SACs (Wu et al., 2020; Yang et al., 2020; Zhang et al., 2019). To date, transition metals like Fe, Cu, and Co have been successfully deposited on different nitrogen-rich supports by forming metal-N_x structures in SACs; in contrast to high-valent metal species, however, radicals were always produced by activating peroxides (Li et al., 2018c; Wu et al., 2020; Yin et al., 2019). Introduction of dopants can tailor the local coordination environment with dispersed metal atoms to enhance SAC performance (Chu et al., 2013; Ong et al., 2016; Wang et al., 2018a). It is also known that the heterolysis of hydroperoxide O–O single bonds and the formation of high-valent Fe species were preferred in electron-deficient rather than electron-rich Fe porphyrin complexes in activating peroxides, and the high-valent Fe species associated with electron-deficient porphyrin ligands had more enhanced reactivity for hydroxylation than those with electron-rich porphyrin ligands (Goh and Nam, 1999; Nam et al., 2000). Therefore, the electronic nature of transition metals is the key for designing SACs to advance the production of high-valent transition metal species.

In this work, we prepared an Fe-based SAC on an oxygen-doped, nitrogen-rich carbon support (SAFe-OCN) that advanced the performance of CEC degradation for water purification. Several CECs were selected to evaluate the catalytic performance of SAFe-OCN by activating PMS, and the contribution of high-valent Fe species (instead of radicals or $^1O_2$) for contaminant degradation was demonstrated. The effects of complex water matrices on catalytic performance and catalyst robustness were also evaluated. Many previous studies have identified the positive impact of Fe on peroxide activation via enhanced adsorption (Chen et al., 2021; Peng et al., 2021; Qian et al., 2021). Instead, we focused on the electronic nature of Fe complexes in the single-atom catalyst, which was largely overlooked before. We found that oxygen-doping in the Fe-nitrogen complexes tailored their frontier orbital energy levels, enabled multiple-electron transfer from the Fe center, and potentially promoted the formation of high-valent Fe species, which could in turn increase the reactivity for contaminant degradation.

To the best of our knowledge, this is the first work that (i) develops the single-atom Fe catalyst to promote multiple-electron-transfer of Fe and possibly high-valent Fe species formation through oxygen-doping and (ii) acknowledges the heterogeneity of the local coordination environment of Fe atoms in experimental characterizations, which could provide a framework for advancing rational catalyst design. Our work also underscores the excellent performance and broad-spectrum applications of SACs for environmental remediation, especially in water and wastewater treatment.

2. Experimental section

2.1. Chemicals

All chemicals are listed in Supplementary Materials (Text S1). They were at least reagent grade and used as received without any treatment.

2.2. Catalyst synthesis

A single-atom Fe catalyst on an oxygen-doped, nitrogen-rich carbon support (SAFe-OCN) was synthesized by heating a mixture of dicyandiamide (DCD), pyromellitic dianhydride (PMDA), and ferric chloride hexahydrate ($FeCl_3 \cdot 6H_2O$) at 325 °C for 4 h. During thermal polycondensation, DCD was converted to a nitrogen-rich carbon support (possibly melem) while electron-deficient PMDA introduced oxygen dopants. An Fe catalyst on carbon nitride support (Fe-CN) and an oxygen-doped, nitrogen-rich carbon support without Fe (OCN) were also fabricated based on previous studies as reference materials (Kofuji et al., 2016, 2017; Li et al., 2018b), which have been systematically characterized before. Details of catalyst development are included in Text S2.

2.3. Catalyst characterizations

X-Ray diffraction (XRD) patterns were collected using an X-ray diffractometer (Panalytical PW-3040 Pro Series) in the range of 2θ = 5–90° with Cu Kα radiation (45 kV/40 mA). Attenuated total reflectance-Fourier transform infrared (ATR-FTIR) spectra were collected using an iS10 Nicolet Thermo ATR-FTIR in the spectral range of 525–4000 cm^{-1}. X-ray photoelectron spectroscopy (XPS) analysis was conducted on a PHI 5600 system with a Mg Ka source (1253.6 eV) under ultrahigh vacuum conditions (pressure < 10^{-8} Torr). The Brunauer-Emmett-Teller (BET) specific surface area and pore size distribution were measured by nitrogen gas (N_2) adsorption-desorption using a Micromeritics ASAP Plus 2020 physisorption analyzer collected for $P_0 P^{-1}$ = 0.01–0.99. Prior to analysis, samples were degassed at 120 °C for 4 h under dynamic vacuum (10^{-2} Torr). The Fe loading in Fe-CN and SAFe-OCN were determined by inductively coupled plasma optical emission spectrometry (ICP-OES). Transmission electron microscopy (TEM) and high-angle annular dark-field scanning transmission electron microscopy with energy dispersive X-ray spectroscopy (HAADF-STEM-EDS) were conducted on a FEI Talos™ F200X scanning transmission electron microscope operated at 200 kV. Aberration-corrected HAADF-STEM (AC-HAADF-STEM) images were taken by a JEOL JEM ARM200F transmission electron microscope operated at 200 kV, equipped with a spherical aberration corrector. The X-ray absorption near-edge structure

(XANES) and extended X-ray absorption fine structure (EXAFS) measurements at Fe *K*-edge were carried in a transmission mode at beamline 20-BM-B. ^{57}Fe Mössbauer spectra were recorded using a spectrometer operated in a constant acceleration mode, equipped with a liquid-helium-cooled, 8DT Janis cryostat fitted with an American Magnetics superconducting coil. More details of catalyst characterizations are included in Text S3.

2.4. Catalytic oxidation for contaminant degradation

All experiments were conducted in sealed and aluminum-foil-packed serum bottles under magnetic stirring at room temperature (500 rpm, 20 °C). A contaminant was introduced to the phosphate buffer (pH 7, 10 mM), then a peroxide (e.g., PMS, peracetic acid (PAA), PDS, or H_2O_2) and a catalyst were added to initiate the catalytic reaction. Samples were withdrawn at different time intervals, filtered through 0.2 μm polyvinylidene difluoride (PVDF) syringe filters and immediately quenched by sodium nitrite ($NaNO_2$, 0.5 M) before further analysis. Contaminant concentrations was analyzed by high performance liquid chromatography (HPLC, Shimadzu LC-20AT Prominence, Kinetex® C18 reverse phase column (50 × 4.6 mm, 2.6 μm particle size), column temperature at 40 °C), and analytical parameters are available in Table S1. The PMS concentration was determined by a colorimetric method with 2,2′-azinobis(3-ethylbenzothiazoline-6-sulfonic acid) diammonium salt (ABTS) by a UV–vis spectrophotometer (GENESYS™ 150). Details of PMS quantification are shown in Text S4. ROS scavengers (i.e., *tert*-butyl alcohol (TBA) for $^{\bullet}$OH, ethanol (EtOH) for both $^{\bullet}$OH and $SO_4^{\bullet-}$, and furfuryl alcohol (FFA) for $^1O_2$) were introduced into catalytic reactions to selectively quench specific ROS and to understand the role of ROS in contaminant degradation. Radicals (e.g., $^{\bullet}$OH, $SO_4^{\bullet-}$, and $O_2^{\bullet-}$) and $^1O_2$ were also detected by electron paramagnetic resonance (EPR) on a Bruker (Billerica, MA) EMX X-band spectrometer at room temperature with 5,5-dimethyl-1-pyrroline-*N*-oxide (DMPO) and 2,2,6,6-tetramethyl-4-piperidinol (TEMP) as the trapping agents, respectively. Methyl phenyl sulfoxide (PMSO) was used for quantifying high-valent Fe species. The concentrations of FFA and PMSO were also quantified by HPLC. To understand the impact of complex water matrices on catalytic performance, inorganic anions (e.g., Cl^- and HCO_3^-) and humic acid that commonly quench ROS were added to the phosphate buffer to evaluate contaminant degradation kinetics. Treated wastewater samples collected from a local wastewater reclamation facility were also used for contaminant degradation. The pseudo-first-order reaction rate constant for the degradation of contaminants, FFA, and PMSO was obtained from the slope of a linear regression of natural logarithm of chemical concentrations versus time. At least duplicates were conducted for batch experiments, and the mean and standard deviation were reported.

2.5. Molecular simulations

For each Fe^{II} complex, its structure was first optimized at its singlet (S = 0), triplet (S = 1), and quintet (S = 2) spin states at the complete active space self-consistent field (CASSCF) level with 8 active electrons and 8 active orbitals denoted as CAS(8,8) (Siegbahn, 1981). Similarly, for the Fe^{III} complex, its optimized structures at doublet (S = 1/2), quartet (S = 3/2), and sextet (S = 5/2) were determined at the CAS(7,8) level. Unless otherwise specified, all simulations were carried out by ORCA quantum chemistry software with def2-TZVP basis set (Weigend and Ahlrichs, 2005; Neese, 2018). Next, the redox centers of those optimized structures were ascertained by examining their electrophilic and nucleophilic Fukui functions, which are defined as $f^-(r) = \rho(N,r) - \rho(N-1,r)$ and $f^+(r) = \rho(N+1,r) - \rho(N,r)$, respectively, where $\rho(N,r)$ is the electron density of a molecule, and $\rho(N-1,r)$ and $\rho(N+1,r)$ are its counterparts when an electron is removed and added, respectively. Finally, we extracted the frontier orbital energies in all Fe complexes at their most stable spin state to compare their relative redox capacity.

3. Results and discussions

3.1. Catalyst characterizations

SAFe-OCN had a low surface area of 1.05 ± 0.10 $m^2\ g^{-1}$ and contained pores with diameter of 19.6 ± 0.8 nm (Table S2 and Fig. S1). The similar surface area and average pore size were shared by SAFe-OCN and OCN, suggesting negligible change in the pore structure after introducing Fe for catalyst synthesis and well-dispersion of Fe species in SAFe-OCN. In the XRD spectra of OCN (Fig. S2), two peaks at $2\theta = 13.5$ and 27.8° could be assigned to the (100) in-plane reflection and the (002) interlayer stacking of graphitic materials, respectively (Fina et al., 2015; Zheng et al., 2016; Li et al., 2018b). XRD spectra of OCN also showed another two peaks at $2\theta = 19.4$ and 29.8° which might arise from the thermal polycondensation of PMDA-PMDA and DCD-PMDA units, respectively (Kofuji et al., 2016). Notably, there was no significant difference between OCN and SAFe-OCN in their XRD patterns, and therefore no new diffractions on SAFe-OCN suggested that Fe was well-dispersed and did not form aggregates such as nanoparticles or microparticles (Yin et al., 2019).

TEM characterization revealed a thin-layered structure of SAFe-OCN without nanoparticles or aggregates (Fig. S3). HAADF-STEM-EDS elemental mapping showed that C, N, O, and Fe elements were uniformly distributed throughout the catalyst (Fig. 1A); specifically, Fe was present as single-atom highlighted in the AC-HAADF-STEM image (Fig. 1B). X-ray absorption spectroscopy (XAS) analysis including XANES and EXAFS were performed to investigate the coordination environment and the chemical state of Fe in SAFe-OCN at the atomic level. The absorption edge of SAFe-OCN in XANES indicated Fe^{II} and/or Fe^{III} could be present in SAFe-OCN (Fig. 1C). The EXAFS spectra of Fe^{II}Pc, FeO, and Fe displayed the peak around 1.50, 1.63, and 2.18 Å individually, which represented the Fe–N, Fe–O, and Fe–Fe bond, respectively (Fig. 1D). Only a large peak centered at 1.59 Å was observed for SAFe-OCN, which could be attributed to the Fe–N or/and Fe–O bond. Most importantly, no Fe–Fe bond was observed in SAFe-OCN, indicating that the isolated and monodispersed Fe atoms were present over the entire catalyst. The quantitative EXAFS fitting was implemented to further investigate the local coordination environment of the Fe atom in SAFe-OCN. As shown in Fig. S4 and Table S3, the fitting curves suggested that a FeN_2O_2 structure (the same structure of O_2-Fe^{II}-N_2 complex in Fig. 5) might represent the active center of SAFe-OCN on average. EXAFS is an ensemble-averaged characterization for a heterogenous sample (Lin et al., 2017), therefore the coordination number with O and N might vary for each Fe atom in SAFe-OCN. The result suggested the heterogeneity of the coordination environment of Fe in SACs.

XPS analysis was also used to evaluate the binding energy and surface concentration of elements (< 10 nm of probing depth) in SAFe-OCN (Fig. 1E). In the C(1s) region, the peak at 284.5 eV was attributed to adventitious carbon or/and graphitic carbon formed during the material calcination process, and the peak at 287.5 eV represented the sp^2 hybridized carbon (i.e., -C-N=C-) (Li et al., 2008). In the N(1s) region, three characteristic peaks observed at 398.5, 400.0, and 404.9 eV represented sp^2 hybridized nitrogen (i.e., -C-N=C-), tertiary nitrogen (i.e., N-$(C)_3$), and π−π* excitations between the graphitic layers, respectively (Ye et al., 2017a; Zheng et al., 2016). In the O(1s) region, a single broad peak centered at 531.5 eV corresponded to -N-C-O- (Wei et al., 2018). In the Fe(2p) region, two peaks consistent with the Fe($2p_{3/2}$/$2p_{1/2}$) doublet were found at 710.1 and 722.4 eV, respectively. Due to the low loading of Fe (Table S4), it was difficult to precisely discern the oxidation state of Fe, though they appear likely a combination of Fe^{II} and Fe^{III}, and are clearly not zero-valent Fe. ATR-FTIR spectra of SAFe-OCN showed bands in 3500–3000 and 1650–1100 cm^{-1} region that represented the stretching of primary (-NH_2) and secondary amines (-NH-), and C-N heterocycles, respectively (Fig. S5) (Li et al., 2018b; Zheng et al., 2016). The results were in good agreement with XPS data. Notably, the

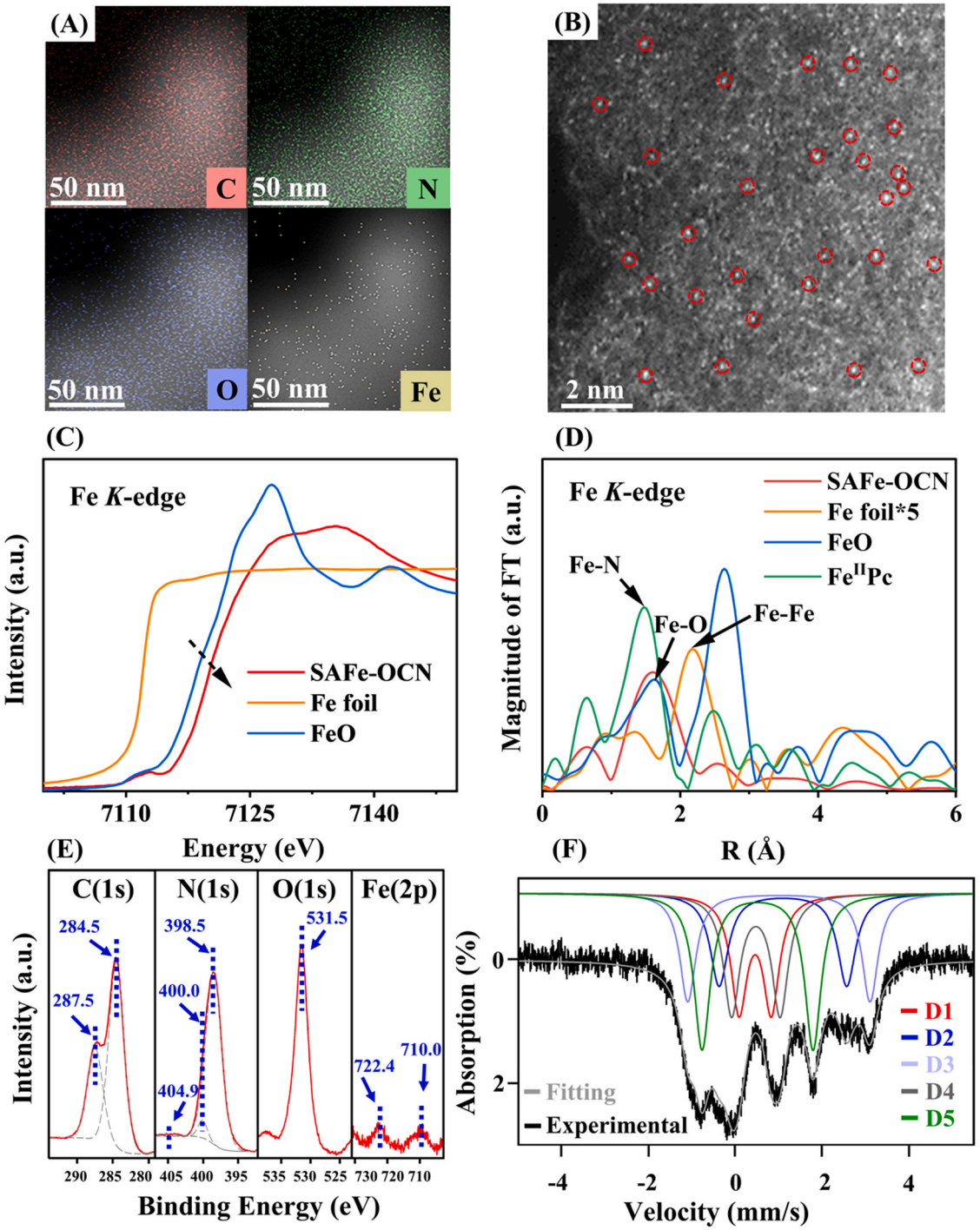

Fig. 1. (A) Elemental distribution of C, N, O, and Fe characterized by HAADF-STEM-EDS mapping and (B) single-atom nature of Fe in SAFe-OCN characterized by AC-HAADF-STEM. (C) XANES spectra and (D) k^3-weighted Fourier transform of EXAFS spectra at Fe *K*-edge of SAFe-OCN and reference materials. (E) XPS spectra of C(1s), N(1s), O(1s), and Fe(2p) in SAFe-OCN. (F) ^{57}Fe Mössbauer spectra of SAFe-OCN.

stretching bands observed at 1717 and 1061 cm^{-1} could be assigned to C=O and C–O bonding, respectively (Kofuji et al., 2017).

^{57}Fe Mössbauer spectroscopy was used to identify the nuclear environment of Fe in SAFe-OCN (Fig. 1F and Table S5). The Mössbauer spectra of SAFe-OCN could be well-fitted with five doublets (e.g., D1-D5). Most Fe was shown as mononuclear high-spin Fe^{II} (quintet, S = 2) species (D2 and D3) and mononuclear high-spin Fe^{III} (sextet, S = 5/2) species (D1) (Gütlich et al., 2011). Mössbauer spectra also revealed the presence of both Fe^{II} (ca. 35 – 61%) and Fe^{III} (ca. 39 – 65%), which is also supported by XANES. Last but not least, Mössbauer spectra, as well as EXAFS fitting, highlighted the heterogeneity of SAFe-OCN, which was largely underrecognized previously (Peng et al., 2021).

3.2. Single-atom Fe catalyst activating peroxides for CEC degradation

Nine CECs shown in Fig. 2A were selected to investigate the broad-spectrum catalytic activity of SAFe-OCN for degrading contaminants by activating PMS at a neutral pH (pH 7). CECs have distinct activities in the SAFe-OCN/PMS system, and their degradation rate constants varied by three orders of magnitude (Fig. 2B). Nevertheless, all CECs except for

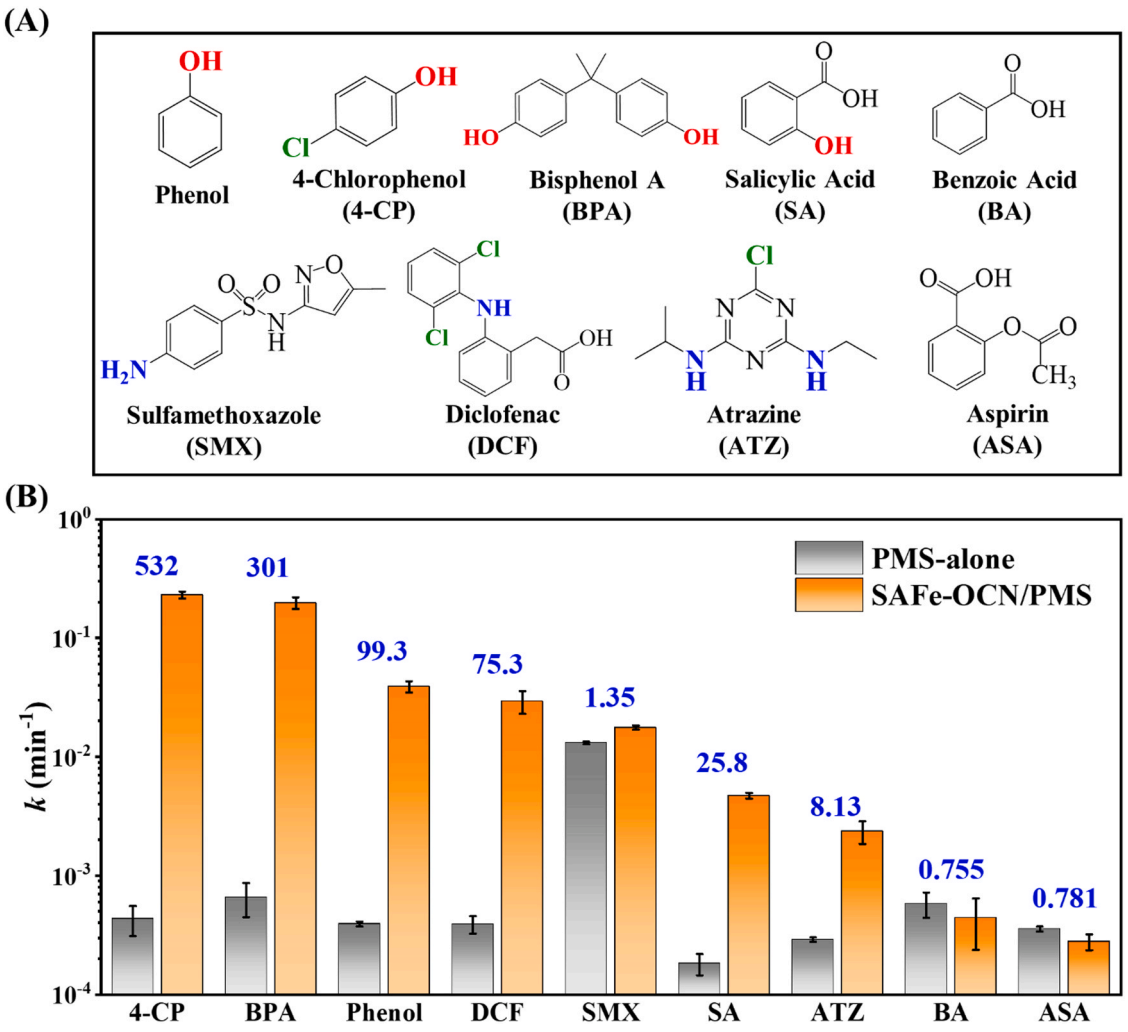

Fig. 2. (A) Chemical structure of CECs. (B) Degradation kinetics of CECs by PMS alone and SAFe-OCN activated PMS (SAFe-OCN/PMS). Columns in (B) represent the first-order reaction rate constant of CEC degradation. Blue numbers in (B) represent the ratio of the first-order reaction rate constants with and without the presence of the SAFe-OCN catalyst. Experimental conditions: initial contaminant concentration of 0.1 mM, initial PMS concentration of 1 mM, SAFe-OCN catalyst loading of 0.5 g L^{-1}, and 10 mM phosphate buffer (pH 7).

sulfamethoxazole (SMX) degraded slowly by the direct oxidation of PMS alone (10^{-4}–10^{-3} min^{-1}). Phenolic contaminants including 4-chlorophenol (4-CP), bisphenol A (BPA), phenol, and salicylic acid (SA) degraded rapidly in the SAFe-OCN/PMS system, especially compared with contaminant degradation only with the presence of PMS: the catalyst of SAFe-OCN promoted degradation kinetics by 532, 300, 99.3, and 25.8 times, respectively (Fig. 2B). In addition, contaminants that contain amino groups were also susceptible to oxidation in the SAFe-OCN/PMS system, diclofenac (DCF), atrazine (ATZ), and SMX showed an increased degradation rate constant by 75.3, 8.14, and 1.35 times, respectively, compared to contaminant degradation with PMS alone. Beyond phenolic and amino functional groups, other groups in the contaminants could also play an important role in determining the catalytic activity. 4-CP, DCF, and ATZ which contain electron-withdrawing moieties such as chlorine were susceptible to catalytic oxidation in the SAFe-OCN/PMS system, while contaminants containing a carboxyl group, such as benzoic acid (BA) and acetylsalicylic acid (ASA), degraded very slowly regardless of the presence of SAFe-OCN. The substrate-selectivity shown in the SAFe-OCN/PMS system suggests that radicals like $^{\bullet}OH$ and $SO_4^{\bullet-}$ may not dominate the oxidation because these radicals are highly reactive and generally non-selective, while it agrees with the observations of contaminant degradation by high valent Fe species to a large extent (Shappell et al., 2008; Luo et al., 2017; Li et al., 2018a, 2018b; Chen et al., 2020). The oxidation performance of high-valent Fe species is strongly related to the ionization potential (IP) of aromatic contaminants, which is affected by the electron donating/-withdrawing abilities of substituted functional groups (Ye et al., 2017b; Li et al., 2018b). For instance, phenolic compounds and aromatic amines with lower IP values experience extensive removal by $Fe^{IV/V}$=O and ferrates ($Fe^{V/VI}$) oxidation (Shappell et al., 2008; Sharma, 2013; Sharma et al., 2015; Li et al., 2018b). Faster oxidation by Fe^{VI} was reported for tetrabromobisphenol A than for BPA, and the phenomenon was similar to 4-CP versus phenol oxidation in our SAFe-OCN/PMS system (Fig. 2B), highlighting the role that halogenation plays in making contaminants more susceptible to oxidation by high-valent Fe species (Yang et al., 2014; Sharma et al., 2015).

In addition to PMS, other peroxides like PAA, H_2O_2, and PDS have also been activated for CEC oxidation (Yin et al., 2019; Jiang et al., 2020). The SAFe-OCN catalyst also activated PAA for degrading phenol, and increased the reaction rate constant by 3.08 times compared to the SAFe-OCN/PMS system (Fig. S6, $(1.20 \pm 0.05) \times 10^{-1}$ and $(3.90 \pm 0.04) \times 10^{-2}$ min^{-1} for the SAFe-OCN/PAA and the SAFe-OCN/PMS system, respectively). Surprisingly, SAFe-OCN was not able to activate H_2O_2 or PDS and no apparent phenol degradation was observed (Fig. S6). The above results could be attributed to different chemical properties of peroxides. Though the peroxide bond in PDS could be more easily

activated from the thermodynamic point of view, due to its lower dissociation energy of the peroxide bond (92 kJ mol^{-1} for PDS) than that in PAA, H_2O_2, and PMS (159, 213, and 377 kJ mol^{-1} for PAA, H_2O_2, and PMS, respectively) (Lee et al., 2020; Wang et al., 2020), it is symmetrical in charge distribution. In contrast, the asymmetrical peroxide bond in PAA and PMS induces a partial positive charge on oxygen at the hydrogen side (R-O-O-H) (Lee et al., 2020). Hence, PAA and PMS are more vulnerable to nucleophilic attack by the catalytic center of Fe in SAFe-OCN, and they can enable oxygen atom transfer to the Fe center and form high-valent Fe species for contaminant oxidation (Lee et al., 2020). Owing to its environmentally benign nature and excellent performance, PAA can be considered as an alternative to PMS for catalytic oxidation of CECs for water and wastewater treatment (Kim and Huang, 2020).

3.3. High-valent Fe species involved contaminant degradation

We first used phenol as the probe compound to illustrate the dominant reactive species and reaction pathway that determined CEC degradation on the SAFe-OCN catalyst. No apparent phenol degradation was observed by PMS treatment alone (Fig. 3A, PMS/phenol), indicating direct oxidation of phenol by PMS was negligible. Phenol adsorption to the catalyst of SAFe-OCN was also not significant (Fig. 3A, SAFe-OCN/phenol). Peroxides including PMS are known to oxidize contaminants via both radical and nonradical pathways (Lee et al., 2020). To determine whether radicals played a critical role in contaminant degradation in the SAFe-OCN/PMS system, we employed scavengers that selectively quench $^{\bullet}OH$ and $SO_4^{\bullet-}$, respectively. TBA and EtOH were introduced to quench contaminant reaction with $^{\bullet}OH$ and both $^{\bullet}OH$ and $SO_4^{\bullet-}$, respectively ($k_{(\bullet OH,\ TBA)} = 6.0 \times 10^8\ M^{-1}\ s^{-1}$, $k_{(\bullet OH,\ EtOH)} = 1.2–2.8 \times 10^9\ M^{-1}\ s^{-1}$, and $k^{\bullet}_{(SO4,\ EtOH)} = 1.6–7.7 \times 10^7\ M^{-1}\ s^{-1}$) (Buxton et al., 1988; Neta et al., 1988; Lian et al., 2017). The addition of an excessive amount of TBA or EtOH did not inhibit phenol degradation, implying that both $^{\bullet}OH$ and $SO_4^{\bullet-}$ were not important for oxidation (Fig. 3A, SAFe-OCN/PMS/phenol/TBA and SAFe-OCN/PMS/phenol/EtOH). Moreover, EPR spectroscopy did not detect the signals of DMPO-$^{\bullet}OH$, DMPO-$SO_4^{\bullet-}$, and DMPO-$O_2^{\bullet-}$ adducts, confirming the absence of $^{\bullet}OH$, $SO_4^{\bullet-}$, and $O_2^{\bullet-}$ (Fig. 4A and B) (Zhao et al., 2001; Li et al., 2018b; Yin et al., 2019). Interestingly, 5,5-dimethyl-1-pyrrolidone-*N*-oxyl (DMPOX) was apparently observed (Fig. 4A and B), indicating that the direct oxidation of DMPO by an unknown oxidant took place in the SAFe-OCN/PMS system (Stan and Daeschel, 2005; Verstraeten et al., 2009; Li et al., 2018b; Jiang et al., 2020).

Many nonradical pathways could exist for contaminant oxidation. To examine whether $^1O_2$ was responsible for phenol degradation in the SAFe-OCN/PMS system, FFA was used as the scavenger for selectively quenching the reaction between phenol and $^1O_2$ ($k^1_{(O2,\ FFA)} = 1.2 \times 10^8\ M^{-1}\ s^{-1}$) (Yun et al., 2018). Introducing FFA into the catalytic system did not inhibit phenol degradation kinetics (Fig. 3A, SAFe-OCN/PMS/phenol/FFA), which suggested that $^1O_2$ did not dominate phenol oxidation. By using TEMP as the spin trap for $^1O_2$ in the EPR analysis, we identified the triplet signals of 2,2,6,6-tetramethyl-4-piperidine-*N*-oxyl (TEMPO) and confirmed the presence of $^1O_2$ in the SAFe-OCN/PMS system (Fig. 4C) (Li et al., 2018b; Pan et al., 2021). However, a similar intensity of TEMPO was observed in the PMS-alone and OCN/PMS systems (Fig. 4C and F). $^1O_2$ may result from PMS self-decomposition in water at circumneutral conditions, which is initiated by SO_5^{2-} attacking HSO_5^- (Zhou et al., 2015; Ruiz et al., 2019). Though $^1O_2$ was present in our SAFe-OCN/PMS system, the previous FFA scavenger test has demonstrated that this ROS did not play an essential role for contaminant oxidation. To further prove this conclusion, a competition study was conducted with the co-existence of phenol and FFA in the SAFe-OCN/PMS system. Based on the degradation kinetics of phenol and FFA, and the second-order rate constants for the reactions of $^1O_2$ with both chemicals, FFA decomposition rate constant would have been 1.05×10^4 times faster than what it showed in our study if $^1O_2$ was the dominant reactive species for oxidation (Fig. S7 and Text S5). This evidence excludes the contribution of $^1O_2$ for contaminant degradation.

Nanocarbon was found to mediate electron-transfer between peroxides and contaminants through the catalyst (Nie et al., 2020); however, OCN did not promote phenol degradation (Fig. 3A, OCN/PMS/phenol), suggesting that OCN itself had a low catalytic activity or it was not reactive. We also compared direct oxidation of DMPO in the SAFe-OCN/PMS and OCN/PMS systems. As shown in Fig. 4D and E, negligible or much less DMPOX were detected in the OCN/PMS system, highlighting that Fe but not OCN determined catalytic oxidation. From all analyses above, we hypothesize that high-valent Fe species may be an important reactive species that determines the catalytic oxidation of contaminants in the SAFe-OCN/PMS system. Many studies have indicated that high-valent Fe species are the reactive species in Fe-based catalytic systems, and we used sulfoxide oxidation to elucidate the key reactive species in our SAFe-OCN/PMS system (Collins and Ryabov, 2017; Li et al., 2018a, 2018b). Sulfoxides, such as PMSO, can be selectively oxidized by the high-valent Fe species to sulfones (e.g., $PMSO_2$) through oxygen atom transfer; however, sulfoxides are oxidized to

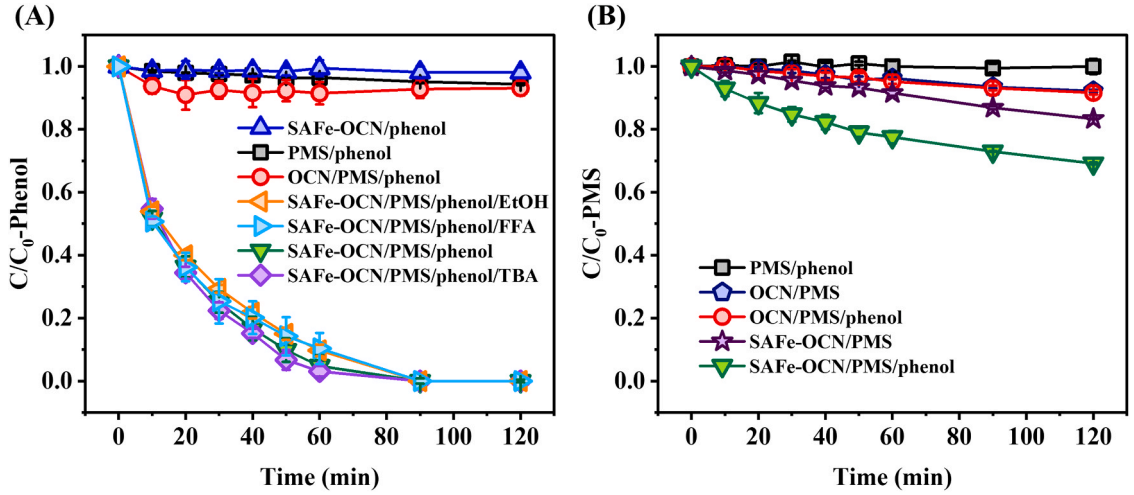

Fig. 3. (A) Phenol degradation and (B) PMS consumption for elucidating the mechanism of using SAFe-OCN for contaminant oxidation. Experimental conditions: initial phenol concentration of 0.1 mM, initial PMS concentration of 1 mM, OCN or SAFe-OCN catalyst loading of 0.5 g L^{-1}, TBA or EtOH concentration of 100 mM, FFA concentration of 2 mM, and 10 mM phosphate buffer (pH 7).

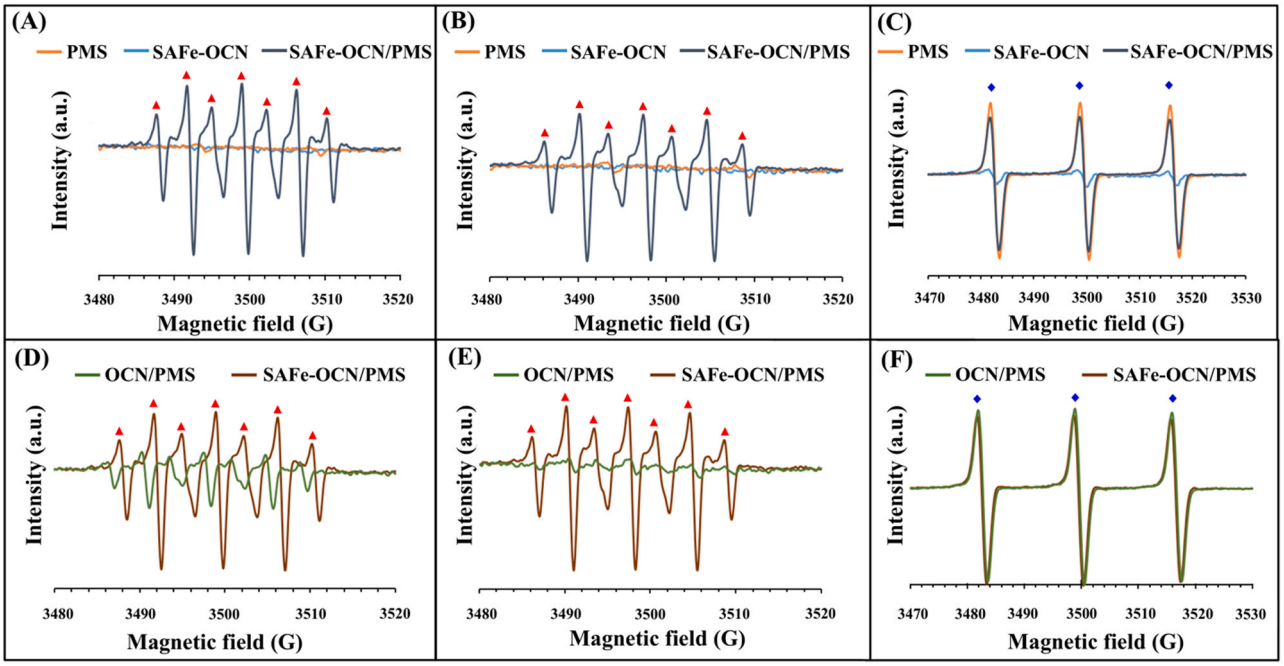

Fig. 4. (A, D) EPR spectra of DMPO adducts in water. Experimental conditions: initial PMS concentration of 1 mM, initial DMPO concentration of 60 mM, OCN or SAFe-OCN catalyst loading of 0.5 g L^{-1}, 10 mM phosphate buffer (pH 7), and reaction time of 1 min (B, E) EPR spectra of DMPO adducts in an ethanol solution. Experimental conditions: initial PMS concentration of 1 mM, initial DMPO concentration of 60 mM, OCN or SAFe-OCN catalyst loading of 0.5 g L^{-1}, 10% (v/v) EtOH, and reaction time of 1 min (C, F) EPR spectra of TEMP adducts in water. Experimental conditions: initial PMS concentration of 1 mM, initial TEMP concentration of 60 mM, OCN or SAFe-OCN catalyst loading of 0.5 g L^{-1}, 10 mM phosphate buffer (pH 7), and reaction time of 1 min.

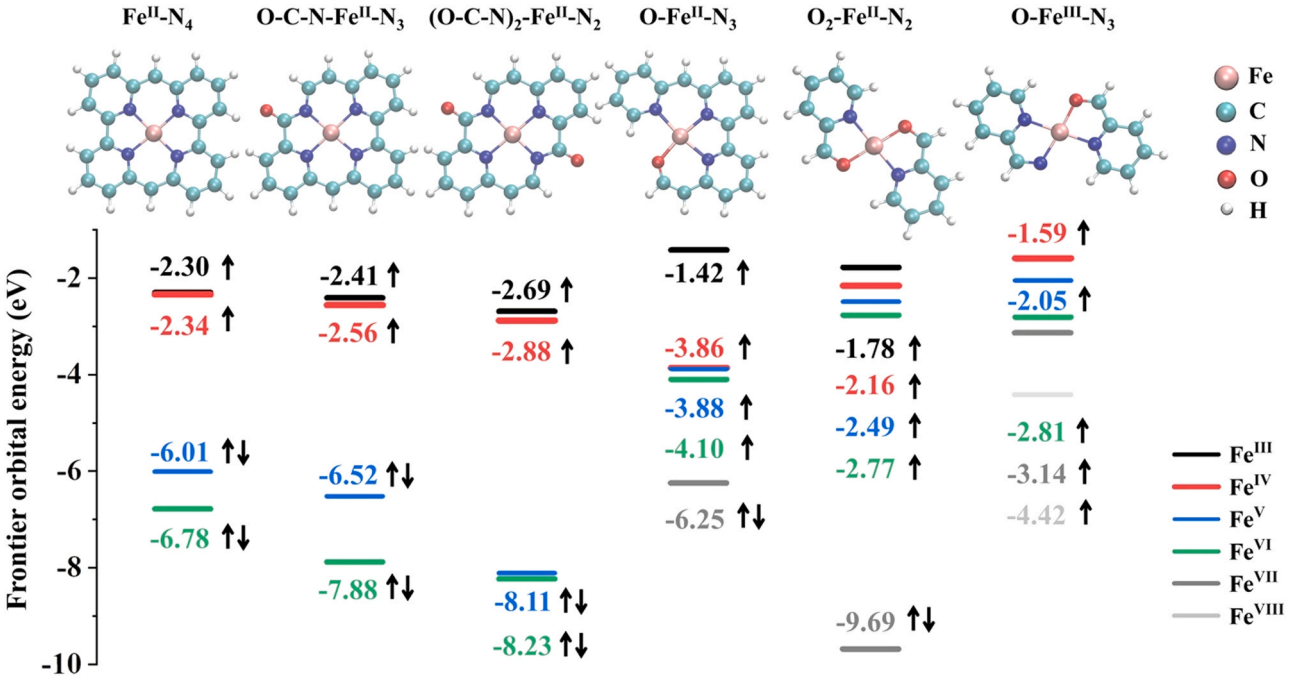

Fig. 5. Molecular structures of Fe^{II}-N$_4$, O-C-N-Fe^{II}-N$_3$, (O-C-N)$_2$-Fe^{II}-N$_2$, O-Fe^{II}-N$_3$, O$_2$-Fe^{II}-N$_2$, and O-Fe^{III}-N$_3$ complexes with their frontier orbital energies.

methyl radical ($^{\bullet}CH_3$) and methanesulfinic acid (CH_3SOOH) in radical-based oxidation (Eberhardt and Colina, 1988; Li et al., 2018b; Wang et al., 2018b; Zhu et al., 2019, 2020). In the SAFe-OCN/PMS system, $PMSO_2$ was produced exclusively from PMSO oxidation at pH 7 and pH 3 based on the mass balance of these two chemicals, which again confirmed that SAFe-OCN/PMS was a radical-free system (Fig. S8A and Fig. S8C). However, PMSO was able to be oxidized to $PMSO_2$ by PMS alone, and no enhancement of reaction kinetics was observed at a neutral pH in the SAFe-OCN/PMS system though the catalyst was present (Fig. S8B). Considering that the self-decomposition and hydrolysis of the high-valent Fe species can be inhibited in acidic conditions, PMSO oxidation was also evaluated at pH 3 to promote the reactivity between the high-valent Fe species and PMSO (Li et al., 2018b; Wang et al., 2018b). Indeed, enhanced reaction kinetics was

observed for PMSO oxidation in the SAFe-OCN/PMS system compared to the PMS-alone system in the acidic condition (1.98-fold increase, Fig. S8D), verifying that the high-valent Fe species are the key species in the SAFe-OCN/PMS system for contaminant oxidation. Contaminant degradation pathway involving high-valent Fe species is highlighted in Scheme 1. However, we could not rule out the contribution of catalyst-mediated electron transfer between the contaminant and PMS for contaminant degradation. Though OCN had negligible reactivity in activating PMS for contaminant degradation, loading of atomically dispersed Fe onto the support of OCN could tailor the electronic structure and conductivity of SAFe-OCN, enhance PMS and contaminant adsorption to the catalyst, and promote the electron-transfer pathway (Yang et al., 2021). Further studies are needed to elucidate the contribution of catalyst-mediated electron transfer for contaminant degradation.

Moreover, PMS consumption rate was analyzed to support our argument that high-valent Fe species played a critical role for contaminant degradation (Fig. 3B). A slight decrease of PMS concentration with a function of time was observed on OCN and the presence of phenol did not promote PMS degradation (Fig. 3B, OCN/PMS and OCN/PMS/phenol), indicating that phenol did not promote the interaction between OCN and PMS and suggested again that OCN-mediated electron transfer was not important (Miao et al., 2020). Interestingly, phenol was not degraded at all in the OCN/PMS system but completely degraded in SAFe-OCN/PMS (Fig. 3A, OCN/PMS/phenol versus SAFe-OCN/PMS/phenol), suggesting Fe again was critical for contaminant oxidation. Moreover, the PMS consumption rate was clearly greater on SAFe-OCN relative to OCN (Fig. 3B, OCN/PMS versus SAFe-OCN/PMS), and the presence of phenol further promoted PMS degradation (Fig. 3B, SAFe-OCN/PMS versus SAFe-OCN/PMS/phenol) due to the fast electron transfer from phenol to the high-valent Fe species (Jiang et al., 2020; Li et al., 2018b). These data demonstrate that Fe was the catalytic center for PMS decomposition, and phenol degradation could be attributed to high-valent Fe species formed at Fe sites on the SAFe-OCN catalyst by activating PMS.

3.4. Electronic nature of Fe in the single-atom catalyst

The electronic nature of central metal atom is critical for determining the catalytic performance of SACs (Goh and Nam, 1999; Nam et al., 2000). As shown in Fig. S9, SAFe-OCN showed 5.13-times faster kinetics of phenol decay than Fe-CN ($(3.90 \pm 0.04) \times 10^{-2}$ versus $(7.60 \pm 1.15) \times 10^{-3}$ min^{-1}), though it had a lower loading of Fe as the catalytic center (0.84 versus 2.55 wt%). To explore whether oxygen-doping plays a critical role in tailoring the electronic nature of FeN_xO_{4-x} structures and promoting catalytic performance, we proposed several FeN_xO_{4-x} complexes with and without oxygen-doping (x = 2, 3, and 4; Fig. 5) to investigate the impact of electron-withdrawing moieties on the redox potential of the central Fe atom in the SACs. Multiple complex structures were selected for molecular simulations to best represent heterogeneous local coordination environments of Fe, which was confirmed by both XAS analysis and Mössbauer spectroscopy.

Fe^{II} is a better reductant than Fe^{III}, and therefore we began our exploration from five Fe^{II} complexes, namely Fe^{II}-N_4, O-C-N-Fe^{II}-N_3, (O-C-N)$_2$-Fe^{II}-N_2, O-Fe^{II}-N_3, and O_2-Fe^{II}-N_2, all with even total number of electrons to meet the multiplicity requirement of Fe^{II} without breaking spin symmetry. For Fe^{II}-N_4, O-C-N-Fe^{II}-N_3, and (O-C-N)$_2$-Fe^{II}-N_2 complexes, triplet was their most stable spin state (Table S6) and they could readily lose two electrons to an oxidant with a reduction potential lower than − 3.0 eV, whereas their highest doubly occupied orbitals were fairly stable below − 6.0 eV (Fig. 5). By contrast, O-Fe^{II}-N_3 and O_2-Fe^{II}-N_2 complexes adopted the quintet spin state (Table S6). The O-Fe^{II}-N_3 complex, was reluctant to lose more than one electron as its second highest singly occupied orbital stayed low at − 3.86 eV, despite a rather high energy of − 1.42 eV for its highest singly occupied orbital (Fig. 5). Interestingly, the O_2-Fe^{II}-N_2 complex, which also adopted the quintet spin state, turned out to be an excellent multiple-electron donor with a narrow range of energy for its first four frontier orbitals lay at − 1.78, − 2.16, − 2.49, and − 2.77 eV, respectively (Fig. 5). The substitution of nitrogen by oxygen for Fe^{II} complexes changed the most stable spin state from triplet to quintet, substantially raising the energy levels of the occupied frontier orbitals, which suggested the importance of electronic structure of the central Fe atom in the SACs. Since Fe^{III} species also exist in SAFe-OCN catalyst, we investigated the O-Fe^{III}-N_3 complex which was formed from O_2-Fe^{II}-N_2 complex by replacing one of its oxygen atoms by nitrogen to attain an odd total number of electrons. In a like manner, the sextet state of the O-Fe^{III}-N_3 complex was more stable than its doublet and quartet counterparts (Table S7), making its first three frontier orbital energies closely located at − 1.59, − 2.05, and − 2.81 eV, respectively (Fig. 5), which were well-aligned with those of O_2-Fe^{II}-N_2 complex. As a result, the oxygen-doping in the SACs is conjectured to greatly facilitate their capacity to donate electrons, and thus making them better reducing agents to form high-valent Fe species by activating PMS, which in turn enhanced phenol degradation kinetics (Fig. S9). Finally, the calculated electrophilic ($f^-(r)$) and nucleophilic ($f^+(r)$) Fukui functions were presented to determine the redox center for the SACs. As shown in Fig. S10, both $f^-(r)$ and $f^+(r)$ of Fe^{II}-N_4 complex were dominantly located at the central Fe atom, confirming it as the catalytic center for electron transfer. In the future, SACs or homogeneous catalysts with well-defined structures and bonding environments will be synthesized, and EPR and ^{57}Fe Mössbauer spectroscopy will be conducted to characterize the oxidation state and the spin state of Fe to support the prediction of molecular simulations.

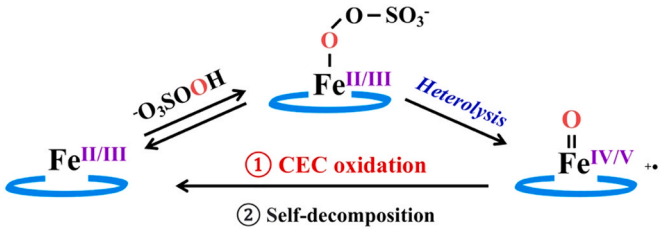

Scheme 1. Proposed mechanism of CEC degradation pathway involving high-valent Fe species in the SAFe-OCN/PMS system.

3.5. Single-atom Fe catalyst being robust in complex environmental matrices

To illustrate whether SAFe-OCN remains active in complex water matrices, we evaluated its catalytic performance for activating PMS and phenol degradation in simulated and real water samples. Negligible inhibition on phenol degradation kinetics was observed with the presence of Cl^- or HCO_3^- (Fig. 6A), which are the common scavengers for radicals, further confirming that neither $^{\bullet}OH$ nor $SO_4^{\bullet-}$ contributed to phenol degradation. In addition, phenol degradation kinetics was less inhibited by humic acid as typical NOM in the SAFe-OCN/PMS system compared to that in a radical-based system (Schellekens et al., 2017). With the presence of humic acid (7.65 mg of total organic carbon (TOC) L^{-1}), phenol degradation kinetics in a radical-based system (Co^{2+}/PMS producing $SO_4^{\bullet-}$ with a steady-state concentration of $(2.51 \pm 0.23) \times 10^{-12}$ M) was inhibited by 2.39 times compared to the scenario without humic acid (Fig. 6B) (Anipsitakis et al., 2006). However, the same concentration of humic acid only led to 46.2% decrease of the phenol degradation rate constant in nonradical-based oxidation by SAFe-OCN (Fig. 6B). Since abundant phenolic groups are present in humic acid substances which could also be susceptible to the degradation by high-valent Fe species, moderate decrease in phenol degradation kinetics was reasonable due to the competition between phenol and humic acid (de Melo et al., 2016; Schellekens et al., 2017). The impact of complex water matrices on the SAFe-OCN/PMS system was also analyzed by using effluents taken from a local water reclamation facility.

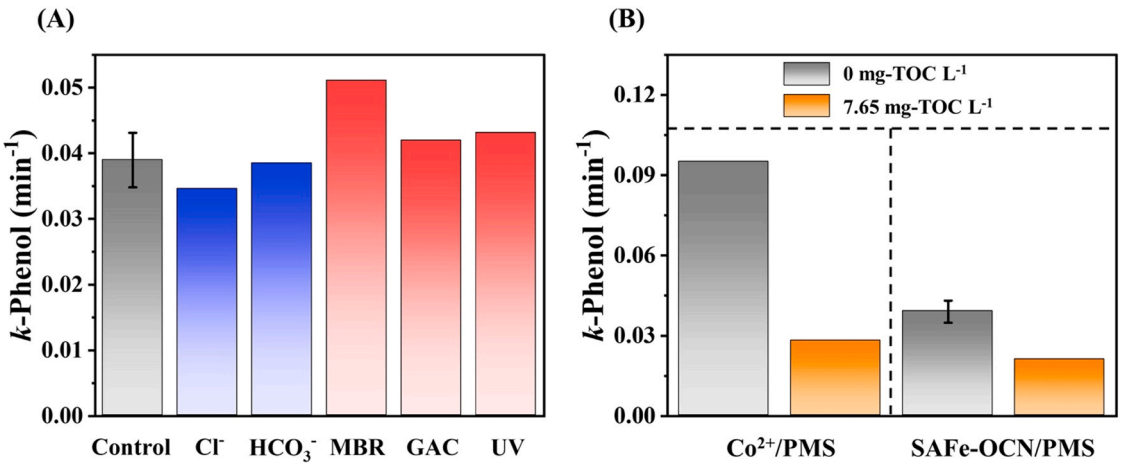

Fig. 6. (A) Effects of complex water matrices on phenol degradation kinetics in the SAFe-OCN/PMS system. The Control (black) column in (A) represents phenol degradation kinetics tested in 10 mM phosphate buffer (pH 7). The blue columns in (A) represent phenol degradation kinetics tested in 10 mM phosphate buffer (pH 7) with the addition of inorganic anions (Cl^- or HCO_3^-). The red columns in (A) represent phenol degradation kinetics tested in treated wastewater samples collected from a local water reclamation facility (i.e., wastewater effluents after membrane bioreactor (MBR) treatment, granular activated carbon (GAC) adsorption, and ultraviolet (UV) disinfection; wastewater treatment processes are highlighted in Fig. S11). Experimental conditions: initial phenol concentration of 0.1 mM, initial PMS concentration of 1 mM, SAFe-OCN catalyst loading of 0.5 g L^{-1}, HCO_3^- concentration of 10 mM, Cl^- concentration of 10 mM, and 10 mM phosphate buffer (pH 7). (B) Effects of humic acid on phenol degradation kinetics in the Co^{2+}/PMS and SAFe-OCN/PMS systems. Experimental conditions: initial phenol concentration of 0.1 mM, initial PMS concentration of 1 mM, SAFe-OCN catalyst loading of 0.5 g L^{-1}, initial Co^{2+} concentration of 0.1 mg L^{-1}, and 10 mM phosphate buffer (pH 7).

Wastewater treatment processes in the water reclamation facility and water quality parameters of effluents after different treatments are shown in Fig. S11 and Table S8, respectively. The catalytic performance of SAFe-OCN for activating PMS and phenol degradation was not inhibited in real water samples when compared to that tested in the phosphate buffer (Fig. 6A), indicating that the SAFe-OCN/PMS system is robust for treating contaminants in practice. The chemical stability of Fe in SAFe-OCN was investigated, and only 0.714% of the total Fe in the catalyst was leached into the solution after reaction. In addition, the stability of SAFe-OCN was also evaluated by degrading phenol for multiple consecutive cycles (Fig. S12). Phenol degradation kinetics was slightly decreased in the second and the third cycle of treatment by 9.72% and 33.4%, respectively, but not in the fourth cycle, highlighting the superior stability of our catalyst for long-term contaminant oxidation.

4. Conclusions

Heterogeneous single-atom catalysis is an emerging research field in recent years, and it attracts attention for environmental remediation including water and wastewater treatment. Heterogeneous single-atom catalysts appear to behave like homogenous catalysts, because of their well-defined structures and because their properties can be readily predicted, designed, and tailored. Our study has developed a single-atom Fe catalyst that forms high-valent Fe species by activating peroxides under circumneutral conditions; the catalyst degrades a broad spectrum of CECs in complex water matrices and is suitable for long-term applications because of its stability. Specifically, the electronic nature of the catalytic center in the single-atom catalyst could be tailored to promote its reactivity for contaminant degradation. Moreover, our catalyst can be readily synthesized from low-cost precursors (such as nitrogen and oxygen rich organics and an earth-abundant transition metal) that potentially allow for scalable and economically feasible implementation. Compared to conventional radical-based AOPs, nonradical-driven single-atom catalysis is robust for water and wastewater treatment in complex water matrices, potentially generates less byproducts, and reduces the energy and chemical footprint to promote the sustainability of contaminant oxidation.

More heterogeneous single-atom catalysts are yet to be designed, developed, and implemented for water and wastewater treatment to enhance the performance of contaminant degradation within nonradical-driven reaction pathways, and they hold promise for the oxidation and reduction of chemical contaminants and disinfection. Future work should focus on optimal catalyst design (e.g., increasing metal loadings but maintaining single-atom dispersion, promoting catalyst surface areas, and fine-tuning of catalyst electronic structures), understanding the mechanism of contaminant transformation, and improving catalyst efficacy (especially contaminant mineralization), selectivity, and robustness for contaminant degradation prior to practical applications.

Both radical-based AOPs and nonradical oxidation on single-atom catalysts have advantages and drawbacks for water and wastewater treatment. It is imperative to understand water chemistry and the susceptibility of contaminants to oxidants before implementing these oxidation processes. For example, radical-based AOPs may be more suitable to oxidize highly persistent contaminants in a relatively clean water matrix, whereas nonradical oxidation may be more preferred to treat contaminants that are susceptible to $^1O_2$, catalyst-mediated electron transfer, or high-valent metal species in complex water matrices. The integration of radical and nonradical oxidation for treating a broad spectrum of contaminants could outperform either oxidation process, including improving contaminant degradation kinetics and mineralization as well as reducing byproduct generation and chemical and energy consumption.

CRediT authorship contribution statement

Zhe Zhou: Conceptualization, Methodology, Formal analysis, Writing - Original Draft, Writing - Review & Editing. **Mengqiao Li**: Investigation. **Chunguang Kuai**: Investigation, Writing - Original Draft. **Yuxin Zhang**: Investigation. **Virginia F. Smith**: Investigation, Writing - Original Draft. **Feng Lin**: Investigation, Writing - Original Draft. **Ashlee Aiello**: Investigation. **David P. Durkin**: Conceptualization, Methodology, Resources, Investigation, Writing - Original Draft. **Hanning Chen**: Conceptualization, Methodology, Resources, Writing - Original Draft, Writing - Review & Editing, Funding acquisition. **Danmeng Shuai**: Conceptualization, Methodology, Resources, Writing - Original Draft, Writing - Review & Editing, Supervision, Project administration, Funding acquisition.

Declaration of Competing Interest

The authors declare that they have no known competing financial interests or personal relationships that could have appeared to influence the work reported in this paper.

Acknowledgments

We acknowledge the National Science Foundation (NSF) grant (CBET – 1932820) for supporting our research. We also acknowledge the Air Force Office of Scientific Research (MIPR #F4FGA08354G001). We thank The George Washington University Nanofabrication and Imaging Center (GWNIC) for TEM and HAADF-STEM-EDS analysis, United States Naval Academy (USNA) for materials characterization (XRD, ATR-FTIR, XPS, N_2 adsorption-desorption) and EPR analysis, and Argonne National Laboratory for XAS analysis. We thank Dr. Sebastian A. Stoian and Adam Valaydon-Pillay in the Department of Chemistry at University of Idaho for ^{57}Fe Mössbauer spectroscopic analysis. We thank Elizabeth Eves in the University of Illinois, Urbana-Champaign for ICP-OES analysis, and Dr. Yue Lin in University of Science and Technology of China for AC-HAADF-STEM imaging. Computational resources were provided by the Argonne Leadership Computing Facilities at Argonne National Laboratory under Department of Energy contract DE-AC-06CH11357 and by the Extreme Science and Engineering Discovery Environment at Texas Advanced Computing Center under NSF contract TG-CHE130008.

Appendix A. Supporting information

Supplementary data associated with this article can be found in the online version at doi:10.1016/j.jhazmat.2021.126294.

References

Anipsitakis, G.P., Dionysiou, D.D., Gonzalez, M.A., 2006. Cobalt-mediated activation of peroxymonosulfate and sulfate radical attack on phenolic compounds. Implications of chloride ions. Environ. Sci. Technol. 40, 1000–1007. https://doi.org/10.1021/es050634b.

Bartolomeu, M., Neves, M., Faustino, M.A.F., Almeida, A., 2018. Wastewater chemical contaminants: remediation by advanced oxidation processes. Photochem. Photobiol. Sci. 17, 1573–1598. https://doi.org/10.1039/c8pp00249e.

Brame, J., Long, M., Li, Q., Alvarez, P., 2015. Inhibitory effect of natural organic matter or other background constituents on photocatalytic advanced oxidation processes: mechanistic model development and validation. Water Res. 84, 362–371. https://doi.org/10.1016/j.watres.2015.07.044.

Buxton, G.V., Greenstock, C.L., Helman, W.P., Ross, A.B., 1988. Critical review of rate constants for reactions of hydrated electrons, hydrogen atoms and hydroxyl radicals ($^{\bullet}OH/^{\bullet}O^{-}$) in aqueous solution. J. Phys. Chem. Ref. Data 17, 513–886. https://doi.org/10.1063/1.555805.

Chen, B.-Y., Kuo, H.-W., Sharma, V.K., Den, W., 2019. Chitosan encapsulation of ferrate (VI) for controlled release to water: mechanistic insights and degradation of organic contaminant. Sci. Rep. 9, 18268. https://doi.org/10.1038/s41598-019-54798-4.

Chen, F., Liu, L.-L., Chen, J.-J., Li, W.-W., Chen, Y.-P., Zhang, Y.-J., Wu, J.-H., Mei, S.-C., Yang, Q., Yu, H.-Q., 2021. Efficient decontamination of organic pollutants under high salinity conditions by a nonradical peroxymonosulfate activation system. Water Res. 191, 116799 https://doi.org/10.1016/j.watres.2020.116799.

Chen, H., Lin, T., Chen, W., Xu, H., Tao, H., 2020. Significant role of high-valent iron-oxo species in the degradation and detoxification of indomethacine. Chemosphere 251. https://doi.org/10.1016/j.chemosphere.2020.126451.

Chen, J., Draksharapu, A., Angelone, D., Unjaroen, D., Padamati, S.K., Hage, R., Swart, M., Duboc, C., Browne, W.R., 2018. H_2O_2 oxidation by Fe(III)-OOH intermediates and its effect on catalytic efficiency. ACS Catal. 8, 9665–9674. https://doi.org/10.1021/acscatal.8b02326.

Chu, S., Wang, Y., Guo, Y., Feng, J., Wang, C., Luo, W., Fan, X., Zou, Z., 2013. Band structure engineering of carbon nitride: in search of a polymer photocatalyst with high photooxidation property. ACS Catal. 3, 912–919. https://doi.org/10.1021/cs4000624.

Collins, T.J., Ryabov, A.D., 2017. Targeting of high-valent iron-TAML activators at hydrocarbons and beyond. Chem. Rev. 117, 9140–9162. https://doi.org/10.1021/acs.chemrev.7b00034.

Cui, X., Li, W., Ryabchuk, P., Junge, K., Beller, M., 2018. Bridging homogeneous and heterogeneous catalysis by heterogeneous single-metal-site catalysts. Nat. Catal. 1, 385–397. https://doi.org/10.1038/s41929-018-0090-9.

de Melo, B.A.G., Motta, F.L., Santana, M.H.A., 2016. Humic acids: structural properties and multiple functionalities for novel technological developments. Mater. Sci. Eng. C 62, 967–974. https://doi.org/10.1016/j.msec.2015.12.001.

Eberhardt, M.K., Colina, R., 1988. The reaction of OH radicals with dimethyl sulfoxide. A comparative study of Fenton's reagent and the radiolysis of aqueous dimethyl sulfoxide solutions. J. Org. Chem. 53, 1071–1074. https://doi.org/10.1021/jo00240a025.

Fasan, R., 2012. Tuning P450 enzymes as oxidation catalysts. ACS Catal. 2, 647–666. https://doi.org/10.1021/cs300001x.

Fina, F., Callear, S.K., Carins, G.M., Irvine, J.T.S., 2015. Structural investigation of graphitic carbon nitride via XRD and neutron diffraction. Chem. Mater. 27, 2612–2618. https://doi.org/10.1021/acs.chemmater.5b00411.

Fu, Q., Malchi, T., Carter, L.J., Li, H., Gan, J., Chefetz, B., 2019. Pharmaceutical and personal care products: from wastewater treatment into agro-food systems. Environ. Sci. Technol. 53, 14083–14090. https://doi.org/10.1021/acs.est.9b06206.

Goh, Y.M., Nam, W., 1999. Significant electronic effect of porphyrin ligand on the reactivities of high-valent iron(IV) oxo porphyrin cation radical complexes. Inorg. Chem. 38, 914–920. https://doi.org/10.1021/ic980989e.

Gupta, S.S., Stadler, M., Noser, C.A., Ghosh, A., Steinhoff, B., Lenoir, D., Horwitz, C.P., Schramm, K.-W., Collins, T.J., 2002. Rapid total destruction of chlorophenols by activated hydrogen peroxide. Science 296, 326–328. https://doi.org/10.1126/science.1069297.

Gütlich, P., Bill, E., Trautwein, A.X., 2011. Mössbauer Spectroscopy and Transition Metal Chemistry: Fundamentals and Application. Springer, Berlin, Heidelberg. https://doi.org/10.1007/978-3-540-88428-6.

Hu, L., Martin, H.M., Strathmann, T.J., 2010. Oxidation kinetics of antibiotics during water treatment with potassium permanganate. Environ. Sci. Technol. 44, 6416–6422. https://doi.org/10.1021/es101331j.

Jiang, N., Xu, H., Wang, L., Jiang, J., Zhang, T., 2020. Nonradical oxidation of pollutants with single-atom-Fe(III)-activated persulfate: Fe(V) being the possible intermediate oxidant. Environ. Sci. Technol. 54, 14057–14065. https://doi.org/10.1021/acs.est.0c04867.

Jiao, L., Yan, H., Wu, Y., Gu, W., Zhu, C., Du, D., Lin, Y., 2020. When nanozymes meet single-atom catalysis. Angew. Chem. Int. Ed. 59, 2565–2576. https://doi.org/10.1002/anie.201905645.

Kaiser, S.K., Chen, Z., Faust Akl, D., Mitchell, S., Perez-Ramirez, J., 2020. Single-atom catalysts across the periodic table. Chem. Rev. 120, 11703–11809. https://doi.org/10.1021/acs.chemrev.0c00576.

Kim, J., Huang, C.-H., 2020. Reactivity of peracetic acid with organic compounds: a critical review. ACS EST Water 1, 15–33. https://doi.org/10.1021/acsestwater.0c00029.

Kofuji, Y., Isobe, Y., Shiraishi, Y., Sakamoto, H., Tanaka, S., Ichikawa, S., Hirai, T., 2016. Carbon nitride-aromatic diimide-graphene nanohybrids: metal-free photocatalysts for solar-to-hydrogen peroxide energy conversion with 0.2% efficiency. J. Am. Chem. Soc. 138, 10019–10025. https://doi.org/10.1021/jacs.6b05806.

Kofuji, Y., Ohkita, S., Shiraishi, Y., Sakamoto, H., Ichikawa, S., Tanaka, S., Hirai, T., 2017. Mellitic triimide-doped carbon nitride as sunlight-driven photocatalysts for hydrogen peroxide production. ACS Sustain. Chem. Eng. 5, 6478–6485. https://doi.org/10.1021/acssuschemeng.7b00575.

Kundu, S., Chanda, A., Khetan, S.K., Ryabov, A.D., Collins, T.J., 2013. TAML activator/peroxide-catalyzed facile oxidative degradation of the persistent explosives trinitrotoluene and trinitrobenzene in micellar solutions. Environ. Sci. Technol. 47, 5319–5326. https://doi.org/10.1021/es4000627.

Lee, J., von Gunten, U., Kim, J.-H., 2020. Persulfate-based advanced oxidation: critical assessment of opportunities and roadblocks. Environ. Sci. Technol. 54, 3064–3081. https://doi.org/10.1021/acs.est.9b07082.

Lee, Y., von Gunten, U., 2010. Oxidative transformation of micropollutants during municipal wastewater treatment: comparison of kinetic aspects of selective (chlorine, chlorine dioxide, ferrate^{VI}, and ozone) and non-selective oxidants (hydroxyl radical). Water Res. 44, 555–566. https://doi.org/10.1016/j.watres.2009.11.045.

Li, H., Shan, C., Li, W., Pan, B., 2018a. Peroxymonosulfate activation by iron(III)-tetraamidomacrocyclic ligand for degradation of organic pollutants via high-valent iron-oxo complex. Water Res. 147, 233–241. https://doi.org/10.1016/j.watres.2018.10.015.

Li, H., Shan, C., Pan, B., 2018b. Fe(III)-doped g-C_3N_4 mediated peroxymonosulfate activation for selective degradation of phenolic compounds via high-valent iron-oxo species. Environ. Sci. Technol. 52, 2197–2205. https://doi.org/10.1021/acs.est.7b05563.

Li, X., Huang, X., Xi, S., Miao, S., Ding, J., Cai, W., Liu, S., Yang, X., Yang, H., Gao, J., Wang, J., Huang, Y., Zhang, T., Liu, B., 2018c. Single cobalt atoms anchored on porous N-doped graphene with dual reaction sites for efficient Fenton-like catalysis. J. Am. Chem. Soc. 140, 12469–12475. https://doi.org/10.1021/jacs.8b05992.

Li, X., Zhang, J., Shen, L., Ma, Y., Lei, W., Cui, Q., Zou, G., 2008. Preparation and characterization of graphitic carbon nitride through pyrolysis of melamine. Appl. Phys. A 94, 387–392. https://doi.org/10.1007/s00339-008-4816-4.

Lian, L., Yao, B., Hou, S., Fang, J., Yan, S., Song, W., 2017. Kinetic study of hydroxyl and sulfate radical-mediated oxidation of pharmaceuticals in wastewater effluents. Environ. Sci. Technol. 51, 2954–2962. https://doi.org/10.1021/acs.est.6b05536.

Lin, F., Liu, Y., Yu, X., Cheng, L., Singer, A., Shpyrko, O.G., Xin, H.L., Tamura, N., Tian, C., Weng, T.-C., Yang, X.-Q., Meng, Y.S., Nordlund, D., Yang, W., Doeff, M.M., 2017. Synchrotron X-ray analytical techniques for studying materials electrochemistry in rechargeable batteries. Chem. Rev. 117, 13123–13186. https://doi.org/10.1021/acs.chemrev.7b00007.

Liu, J., 2017. Catalysis by supported single metal atoms. ACS Catal. 7, 34–59. https://doi.org/10.1021/acscatal.6b01534.

Luo, S., Wei, Z., Dionysiou, D.D., Spinney, R., Hu, W.-P., Chai, L., Yang, Z., Ye, T., Xiao, R., 2017. Mechanistic insight into reactivity of sulfate radical with aromatic

contaminants through single-electron transfer pathway. Chem. Eng. J. 327, 1056–1065. https://doi.org/10.1016/j.cej.2017.06.179.
Marin, M.L., Santos-Juanes, L., Arques, A., Amat, A.M., Miranda, M.A., 2012. Organic photocatalysts for the oxidation of pollutants and model compounds. Chem. Rev. 112, 1710–1750. https://doi.org/10.1021/cr2000543.
Mawhinney, D.B., Young, R.B., Vanderford, B.J., Borch, T., Snyder, S.A., 2011. Artificial sweetener sucralose in U.S. drinking water systems. Environ. Sci. Technol. 45, 8716–8722. https://doi.org/10.1021/es202404c.
Miao, J., Geng, W., Alvarez, P.J.J., Long, M., 2020. 2D N-doped porous carbon derived from polydopamine-coated graphitic carbon nitride for efficient nonradical activation of peroxymonosulfate. Environ. Sci. Technol. 54, 8473–8481. https://doi.org/10.1021/acs.est.0c03207.
Nam, W., Han, H.J., Oh, S.-Y., Lee, Y.J., Choi, M.-H., Han, S.-Y., Kim, C., Woo, S.K., Shin, W., 2000. New insights into the mechanisms of O-O bond cleavage of hydrogen peroxide and tert-alkyl hydroperoxides by iron(III) porphyrin complexes. J. Am. Chem. Soc. 122, 8677–8684. https://doi.org/10.1021/ja994403e.
Neese, F., 2018. Software update: the ORCA program system, version 4.0. WIREs Comput. Mol. Sci. 8, 1–6. https://doi.org/10.1002/wcms.1327.
Neta, P., Huie, R.E., Ross, A.B., 1988. Rate constants for reactions of inorganic radicals in aqueous-solution. J. Phys. Chem. Ref. Data 17, 1027–1284. https://doi.org/10.1063/1.555808.
Nie, C., Dai, Z., Liu, W., Duan, X., Wang, C., Lai, B., Ao, Z., Wang, S., An, T., 2020. Criteria of active sites in nonradical persulfate activation process from integrated experimental and theoretical investigations: boron-nitrogen-co-doped nanocarbon-mediated peroxydisulfate activation as an example. Environ. Sci. Nano 7, 1899–1911. https://doi.org/10.1039/D0EN00347F.
Nosaka, Y., Nosaka, A.Y., 2017. Generation and detection of reactive oxygen species in photocatalysis. Chem. Rev. 117, 11302–11336. https://doi.org/10.1021/acs.chemrev.7b00161.
O'Shea, K.E., Dionysiou, D.D., 2012. Advanced oxidation processes for water treatment. J. Phys. Chem. Lett. 3, 2112–2113. https://doi.org/10.1021/jz300929x.
Oh, W.-D., Dong, Z., Lim, T.-T., 2016. Generation of sulfate radical through heterogeneous catalysis for organic contaminants removal: current development, challenges and prospects. Appl. Catal. B 194, 169–201. https://doi.org/10.1016/j.apcatb.2016.04.003.
Ong, W.-J., Tan, L.-L., Ng, Y.H., Yong, S.-T., Chai, S.-P., 2016. Graphitic Carbon Nitride ($g\text{-}C_3N_4$)-based photocatalysts for artificial photosynthesis and environmental remediation: are we a step closer to achieving sustainability? Chem. Rev. 116, 7159–7329. https://doi.org/10.1021/acs.chemrev.6b00075.
Pan, L., Shi, W., Sen, T., Wang, L., Zhang, J., 2021. Visible light-driven selective organic degradation by $FeTiO_3$/persulfate system: the formation and effect of high valent Fe (IV). Appl. Catal. B Environ. 280, 119414 https://doi.org/10.1016/j.apcatb.2020.119414.
Patel, M., Kumar, R., Kishor, K., Mlsna, T., Pittman, C.U., Mohan, D., 2019. Pharmaceuticals of emerging concern in aquatic systems: chemistry, occurrence, effects, and removal methods. Chem. Rev. 119, 3510–3673. https://doi.org/10.1021/acs.chemrev.8b00299.
Peng, L., Duan, X., Shang, Y., Gao, B., Xu, X., 2021. Engineered carbon supported single iron atom sites and iron clusters from Fe-rich Enteromorpha for Fenton-like reactions via nonradical pathways. Appl. Catal. B 287. https://doi.org/10.1016/j.apcatb.2021.119963.
Qian, K., Chen, H., Li, W., Ao, Z., Wu, Y.-N., Guan, X., 2021. Single-atom Fe catalyst outperforms its homogeneous counterpart for activating peroxymonosulfate to achieve effective degradation of organic contaminants. Environ. Sci. Technol. 55, 7034–7043. https://doi.org/10.1021/acs.est.0c08805.
Rana, S., Dey, A., Maiti, D., 2015. Mechanistic elucidation of C-H oxidation by electron rich non-heme iron(IV)-oxo at room temperature. Chem. Commun. 51, 14469–14472. https://doi.org/10.1039/c5cc04803f.
Ruiz, M., Yang, Y., Lochbaum, C.A., Delafield, D.G., Pignatello, J.J., Li, L., Pedersen, J.A., 2019. Peroxymonosulfate oxidizes amino acids in water without activation. Environ. Sci. Technol. 53, 10845–10854. https://doi.org/10.1021/acs.est.9b01322.
Schellekens, J., Buurman, P., Kalbitz, K., van Zomeren, A., Vidal-Torrado, P., Cerli, C., Comans, R.N.J., 2017. Molecular features of humic acids and fulvic acids from contrasting environments. Environ. Sci. Technol. 51, 1330–1339. https://doi.org/10.1021/acs.est.6b03925.
Shannon, M.A., Bohn, P.W., Elimelech, M., Georgiadis, J.G., Marinas, B.J., Mayes, A.M., 2008. Science and technology for water purification in the coming decades. Nature 452, 301–310. https://doi.org/10.1038/nature06599.
Shappell, N.W., Vrabel, M.A., Madsen, P.J., Harrington, G., Billey, L.O., Hakk, H., Larsen, G.L., Beach, E.S., Horwitz, C.P., Ro, K., Hunt, P.G., Collins, T.J., 2008. Destruction of estrogens using Fe-TAML/peroxide catalysis. Environ. Sci. Technol. 42, 1296–1300. https://doi.org/10.1021/es7022863.
Sharma, V.K., 2013. Ferrate(VI) and ferrate(V) oxidation of organic compounds: kinetics and mechanism. Coord. Chem. Rev. 257, 495–510. https://doi.org/10.1016/j.ccr.2012.04.014.
Sharma, V.K., Chen, L., Zboril, R., 2015. Review on high valent Fe^{VI} (ferrate): a sustainable green oxidant in organic chemistry and transformation of pharmaceuticals. ACS Sustain. Chem. Eng. 4, 18–34. https://doi.org/10.1021/acssuschemeng.5b01202.
Siegbahn, P.E.M., 1981. The complete active space SCF (CASSCF) method in a Newton-Raphson formulation with application to the HNO molecule. J. Chem. Phys. 74, 2384–2396. https://doi.org/10.1063/1.3382344.
Stan, S.D., Daeschel, M.A., 2005. 5,5-Dimethyl-2-pyrrolidone-N-oxyl formation in electron spin resonance studies of electrolyzed NaCl solution using 5,5-dimethyl-1-pyrroline-N-oxide as a spin trapping agent. J. Agric. Food Chem. 53, 4906–4910. https://doi.org/10.1021/jf047918k.
Ternes, T.A., Meisenheimer, M., McDowell, D., Sacher, F., Brauch, H.J., Haist-Gulde, B., Preuss, G., Wilme, U., Zulei-Seibert, N., 2002. Removal of pharmaceuticals during drinking water treatment. Environ. Sci. Technol. 36, 3855–3863. https://doi.org/10.1021/es015757k.
Verstraeten, S.V., Lucangioli, S., Galleano, M., 2009. ESR characterization of thallium (III)-mediated nitrones oxidation. Inorg. Chim. Acta 362, 2305–2310. https://doi.org/10.1016/j.ica.2008.10.013.
Wang, A., Li, J., Zhang, T., 2018a. Heterogeneous single-atom catalysis. Nat. Rev. Chem. 2, 65–81. https://doi.org/10.1038/s41570-018-0010-1.
Wang, C., Kim, J., Malgras, V., Na, J., Lin, J., You, J., Zhang, M., Li, J., Yamauchi, Y., 2019. Metal-organic frameworks and their derived materials: emerging catalysts for a sulfate radicals-based advanced oxidation process in water purification. Small 1900744, 1–21. https://doi.org/10.1002/smll.201900744.
Wang, J., Wang, S., 2016. Removal of pharmaceuticals and personal care products (PPCPs) from wastewater: a review. J. Environ. Manag. 182, 620–640. https://doi.org/10.1016/j.jenvman.2016.07.049.
Wang, Z., Jiang, J., Pang, S., Zhou, Y., Guan, C., Gao, Y., Li, J., Yang, Y., Qiu, W., Jiang, C., 2018b. Is sulfate radical really generated from peroxydisulfate activated by iron(II) for environmental decontamination? Environ. Sci. Technol. 52, 11276–11284. https://doi.org/10.1021/acs.est.8b02266.
Wang, Z., Wang, J., Xiong, B., Bai, F., Wang, S., Wan, Y., Zhang, L., Xie, P., Wiesner, M. R., 2020. Application of cobalt/peracetic acid to degrade sulfamethoxazole at neutral condition: efficiency and mechanisms. Environ. Sci. Technol. 54, 464–475. https://doi.org/10.1021/acs.est.9b04528.
Wei, F., Liu, Y., Zhao, H., Ren, X., Liu, J., Hasan, T., Chen, L., Li, Y., Su, B.-L., 2018. Oxygen self-doped $g\text{-}C_3N_4$ with tunable electronic band structure for unprecedentedly enhanced photocatalytic performance. Nanoscale 10, 4515–4522. https://doi.org/10.1039/c7nr09660g.
Weigend, F., Ahlrichs, R., 2005. Balanced basis sets of split valence, triple zeta valence and quadruple zeta valence quality for H to Rn: design and assessment of accuracy. Phys. Chem. Chem. Phys. 7, 3297–3305. https://doi.org/10.1039/b508541a.
Wojnarovits, L., Toth, T., Takacs, E., 2020. Rate constants of carbonate radical anion reactions with molecules of environmental interest in aqueous solution: a review. Sci. Total Environ. 717. https://doi.org/10.1016/j.scitotenv.2020.137219.
Wu, Q., Wang, J., Wang, Z., Xu, Y., Xing, Z., Zhang, X., Guan, Y., Liao, G., Li, X., 2020. High-loaded single Cu atoms decorated on N-doped graphene for boosting Fenton-like catalysis under neutral pH. J. Mater. Chem. A 8, 13685–13693. https://doi.org/10.1039/d0ta04943c.
Yan, H., Su, C., He, J., Chen, W., 2018. Single-atom catalysts and their applications in organic chemistry. J. Mater. Chem. A 6, 8793–8814. https://doi.org/10.1039/c8ta01940a.
Yang, B., Ying, G.-G., Chen, Z.F., Zhao, J.-L., Peng, F.-Q., Chen, X.-W., 2014. Ferrate(VI) oxidation of tetrabromobisphenol A in comparison with bisphenol A. Water Res. 62, 211–219. https://doi.org/10.1016/j.watres.2014.05.056.
Yang, T., Fan, S., Li, Y., Zhou, Q., 2021. Fe-N/C single-atom catalysts with high density of $Fe\text{-}N_x$ sites toward peroxymonosulfate activation for high-efficient oxidation of bisphenol A: electron-transfer mechanism. Chem. Eng. J. 419 (129590) https://doi.org/10.1016/j.cej.2021.129590.
Yang, Y., Zeng, G., Huang, D., Zhang, C., He, D., Zhou, C., Wang, W., Xiong, W., Song, B., Yi, H., Ye, S., Ren, X., 2020. In situ grown single-atom cobalt on polymeric carbon nitride with bidentate ligand for efficient photocatalytic degradation of refractory antibiotics. Small 12001634, 1–12. https://doi.org/10.1002/smll.202001634.
Ye, T., Durkin, D.P., Banek, N.A., Wagner, M.J., Shuai, D., 2017a. Graphitic carbon nitride supported ultrafine Pd and Pd-Cu catalysts: enhanced reactivity, selectivity, and longevity for nitrite and nitrate hydrogenation. ACS Appl. Mater. Interfaces 9, 27421–27426. https://doi.org/10.1021/acsami.7b09192.
Ye, T., Wei, Z., Spinney, R., Dionysiou, D.D., Luo, S., Chai, L., Yang, Z., Xiao, R., 2017b. Quantitative structure–activity relationship for the apparent rate constants of aromatic contaminants oxidized by ferrate (VI). Chem. Eng. J. 317, 258–266. https://doi.org/10.1016/j.cej.2017.02.061.
Yin, Y., Shi, L., Li, W., Li, X., Wu, H., Ao, Z., Tian, W., Liu, S., Wang, S., Sun, H., 2019. Boosting Fenton-like reactions via single atom Fe catalysis. Environ. Sci. Technol. 53, 11391–11400. https://doi.org/10.1021/acs.est.9b03342.
Yun, E.-T., Lee, J.H., Kim, J., Park, H.-D., Lee, J., 2018. Identifying the nonradical mechanism in the peroxymonosulfate activation process: singlet oxygenation versus mediated electron transfer. Environ. Sci. Technol. 52, 7032–7042. https://doi.org/10.1021/acs.est.8b00959.
Zhang, J., Zhao, Y., Chen, C., Huang, Y.-C., Dong, C.-L., Chen, C.-J., Liu, R.-S., Wang, C., Yan, K., Li, Y., Wang, G., 2019. Tuning the coordination environment in single-atom catalysts to achieve highly efficient oxygen reduction reactions. J. Am. Chem. Soc. 141, 20118–20126. https://doi.org/10.1021/jacs.9b09352.
Zhao, H., Joseph, J., Zhang, H., Karoui, H., Kalyanaraman, B., 2001. Synthesis and biochemical applications of a solid cyclic nitrone spin trap: a relatively superior trap for detecting superoxide anions and glutathiyl radicals. Free Radic. Biol. Med. 31, 599–606. https://doi.org/10.1016/S0891-5849(01)00619-0.
Zheng, Q., Durkin, D.P., Elenewski, J.E., Sun, Y., Banek, N.A., Hua, L., Chen, H., Wagner, M.J., Zhang, W., Shuai, D., 2016. Visible-light-responsive graphitic carbon nitride: rational design and photocatalytic applications for water treatment. Environ. Sci. Technol. 50, 12938–12948. https://doi.org/10.1021/acs.est.6b02579.
Zhou, Y., Jiang, J., Gao, Y., Ma, J., Pang, S.-Y., Li, J., Lu, X.-T., Yuan, L.-P., 2015. Activation of peroxymonosulfate by benzoquinone: a novel nonradical oxidation

process. Environ. Sci. Technol. 49, 12941–12950. https://doi.org/10.1021/acs.est.5b03595.

Zhu, J., Yu, F., Meng, J., Shao, B., Dong, H., Chu, W., Cao, T., Wei, G., Wang, H., Guan, X., 2020. Overlooked role of Fe(IV) and Fe(V) in organic contaminant oxidation by Fe(VI). Environ. Sci. Technol. 54, 9702–9710. https://doi.org/10.1021/acs.est.0c03212.

Zhu, Z., Lu, W., Xu, T., Li, N., Wang, G., Chen, W., 2019. High-valent iron-oxo complexes as dominant species to eliminate pharmaceuticals and chloride-containing intermediates by the activation of peroxymonosulfate under visible Iirradiation. Catal. Lett. 150, 1355–1367. https://doi.org/10.1007/s10562-019-03047-4.